ACS OMEGA

Open Access

http://pubs.acs.org/journal/acsodf

Article

Simultaneous Growth Strategy of High-Optical-Efficiency GaN NWs on a Wide Range of Substrates by Pulsed Laser Deposition

Dhaifallah Almalawi,[▽] Sergei Lopatin, Paul R. Edwards, Bin Xin, Ram C. Subedi, Mohammed A. Najmi, Fatimah Alreshidi, Alessandro Genovese, Daisuke Iida, Nimer Wehbe, Boon S. Ooi, Kazuhiro Ohkawa, Robert W. Martin, and Iman S. Roqan*,[▽]

Cite This: *ACS Omega* 2023, 8, 46804−46815

Read Online

ACCESS | Metrics & More | Article Recommendations | Supporting Information

ABSTRACT: Here, we explore a catalyst-free single-step growth strategy that results in high-quality self-assembled single-crystal vertical GaN nanowires (NWs) grown on a wide range of common and novel substrates (including GaN, Ga_2O_3, and monolayer two-dimensional (2D) transition-metal dichalcogenide (TMD)) within the same chamber and thus under identical conditions by pulsed laser deposition. High-resolution transmission electron microscopy and scanning transmission electron microscopy (HR-STEM) and grazing incidence X-ray diffraction measurements confirm the single-crystalline nature of the obtained NWs, whereas advanced optical and cathodoluminescence measurements provide evidence of their high optical quality. Further analyses reveal that the growth is initiated by an *in situ* polycrystalline layer formed between the NWs and substrates during growth, while as its thickness increases, the growth mode transforms into single-crystalline NW nucleation. HR-STEM and corresponding energy-dispersive X-ray compositional analyses indicate possible growth mechanisms. All samples exhibit strong band edge UV emission (with a negligible defect band) dominated by radiative recombination with a high optical efficiency (~65%). As all NWs have similar structural and optical qualities irrespective of the substrate used, this strategy will open new horizons for developing III-nitride-based devices.

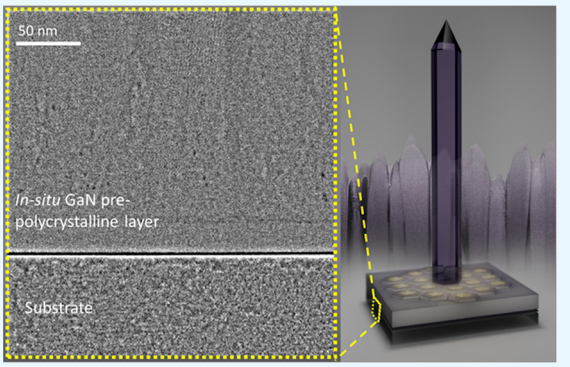

1. INTRODUCTION

III-nitride semiconductors, GaN-based materials, in particular, already have a wide range of high-power[1] and high-frequency[2] optoelectronic and electronic applications, such as energy-saving light-emitting[3] and transistor devices,[4] photoelectrochemical water-splitting devices for energy generation,[5] and devices used for sensing and medical curing, as well as those operating in harsh industrial environments. The extensive use of these materials is motivated by their inherent outstanding properties, such as the direct and tunable band gap, excellent thermal stability, and mechanical durability.[6] Rapid technological advances, along with the emergence of novel GaN-based applications, such as flexible displays,[7] biosensors,[8] and vertical-cavity surface-emitting lasers (VCSELs),[9] have increased the demand for high-quality GaN growth on a wide range of potential substrates. While this practical goal must be achieved for mass production, the direct GaN growth of sufficient quality on any emerging, affordable, or fixable substrates remains challenging in practice.

In this process, the main issue pertains to the large lattice mismatch between the common substrates (such as Si, SiC, and sapphire) and III-nitride materials, which induces extended threading dislocations (TDs) at the substrate interface that create nonradiative centers,[10] resulting in low internal quantum efficiency (IQE) and hence low external efficiency. Moreover, problems arising from thermal expansion differences or the high cost and size limitation of some potential and common substrates restricted the fabrication of possible applications and increased the cost.[11] For example, GaN substrates have been shown to be effective in eliminating TD defects,[12] but this approach is extremely expensive and is thus not suited for large-scale applications.

Even though a wide range of strategies have been proposed to overcome these limitations, most researchers advocate the use of III-nitride nanowires (NWs) as a potential solution for high TD density issues.[13,14] In the NW structure, the density of TDs that propagate across the interface into the NWs is reduced substantially as the small NW diameter promotes an elastic strain relaxation mechanism, resulting in the formation of TD-free NWs. NW growth has been successfully achieved using different substrates, including two-dimensional (2D)

Received: August 24, 2023
Revised: November 2, 2023
Accepted: November 6, 2023
Published: December 1, 2023

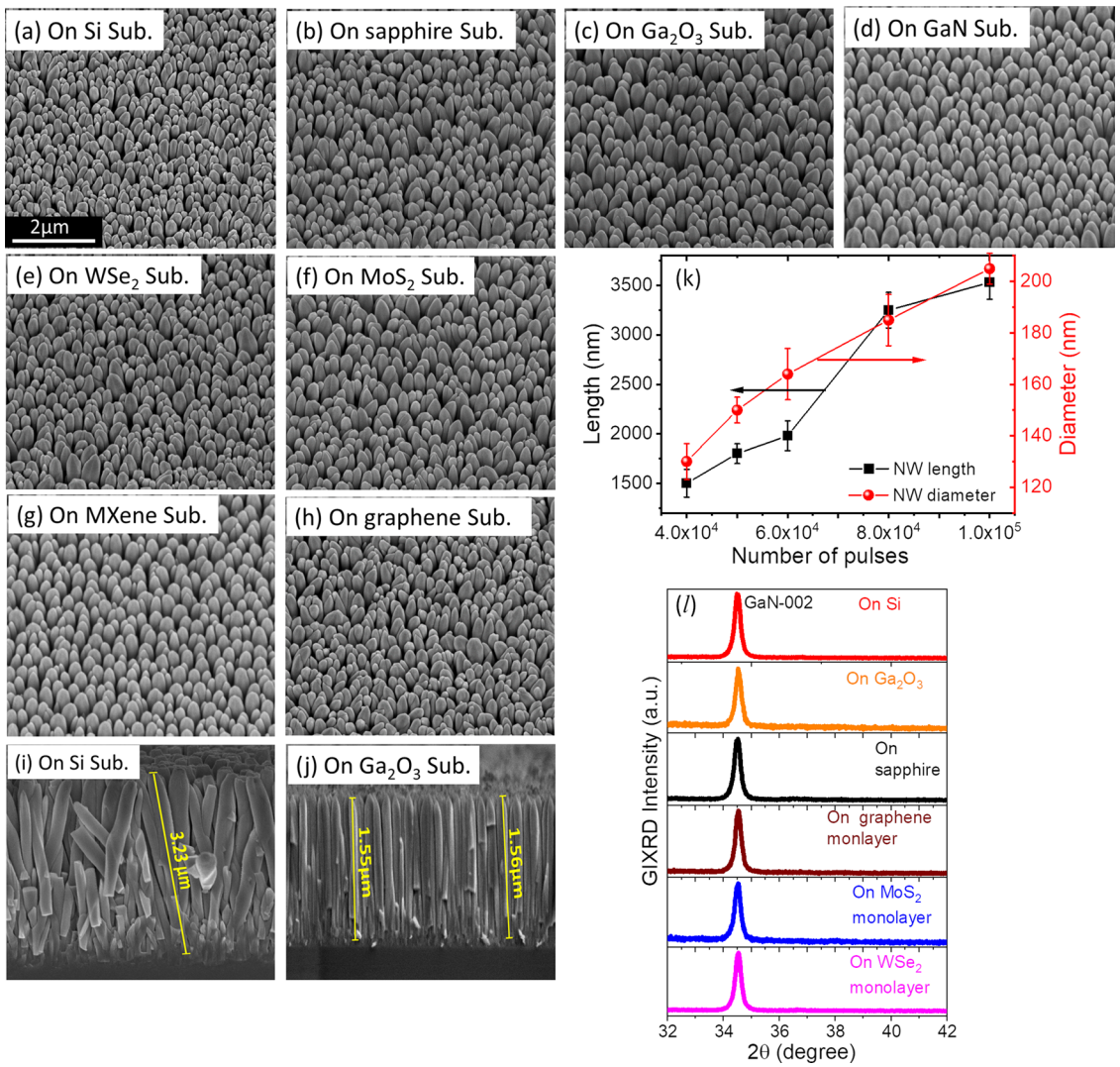

Figure 1. (a–h) Tilted-view SEM images of self-assembled GaN NWs grown on different substrates (using identical conditions). Cross-sectional SEM images of GaN NWs grown on (i) Si and (j) (−201) β-Ga_2O_3 were achieved under the optimal conditions while varying the number of pulses (40,000 and 100,000 pulses, respectively). (k) The dependence of the number of pulses of NW length and diameter when all conditions remain constant. (l) GIXRD patterns for GaN NWs grown on all substrates.

materials (e.g., graphene,[15] boron nitride,[16] and multiple MoS_2 layers[16,17]), polycrystalline substrates, and buffer interlayers (e.g., MXene[17] or Ti[18]). However, all strategies proposed thus far for optimizing the GaN growth conditions are substrate-dependent. As a result, some promising substrates, such as Ga_2O_3 and monolayer 2D transition-metal dichalcogenide (TMD), have not been successfully used thus far to obtain GaN NWs of sufficient quality. Thus, due to this substrate issue, the lift-off and flip-chip processes[19] were used to transfer the device to a desirable substrate, thus further increasing the design complexity.

On the other hand, as a part of our previous work, we demonstrated that catalyst-free high-quality ZnO NWs and nanotubes can be grown on different substrates (including GaN) by precisely controlling the pulsed laser deposition (PLD) conditions,[20,21] which is considered a relatively cost-effective technique compared to the common GaN growth techniques.

In this work, our aim is to achieve a high-quality GaN NW growth strategy irrespective of the substrate type. For this purpose, we developed a facile and relatively inexpensive growth strategy and applied it to obtain self-assembled vertical GaN NWs grown directly on a wide range of bulk and 2D substrates simultaneously using the PLD method without a catalyst. The major advantage of this approach stems from eliminating the substrate influence on the GaN NW quality and growth procedure. Advanced structural analyses reveal the mechanism of such an NW growth method, while the optical characterizations confirm the optical and structural quality of the resulting NWs.

2. GROWTH AND EXPERIMENTAL METHODS

A Pioneer 240 PLD system (Neocera) equipped with a KrF excimer laser (248 nm line) was used to ablate a commercial GaN target of 99.95% purity that was doped unintentionally with oxygen during target synthesis. To grow vertical GaN NWs on different substrates simultaneously, the target was exposed to the laser beam to ablate the species toward substrates. The following settings were utilized to form NWs, as they were experimentally determined to yield the most optimal growth conditions: 150–250 mTorr nitrogen pressure (P_{N_2}); 0.95–1.05 J·cm^{-2} beam fluence focused on the GaN

https://doi.org/10.1021/acsomega.3c06302
ACS Omega 2023, 8, 46804−46815

target surface; 8.5−9 cm vertical distance (d) between the substrate and the target; and 850 °C growth temperature (T), with a minimum of 40,000 laser pulses at a 10 Hz laser repetition rate. Different substrates were placed in the chamber at the same time, namely, a single-side-polished p-type Si (100) (from University Wafer Inc.); a single-layer graphene/90 nm SiO_2/highly (100) p-doped Si wafer (from α Graphene Inc.); a commercial bulk (−201) β-Ga_2O_3 (from Novel Crystal Co.); a Mg-doped GaN (p-GaN) template grown on c-sapphire substrate (from University Wafer Inc.); a c-sapphire (from Semiconductor Wafer Inc.); and Ti_3C_2 MXene with an ∼40 μm particle size (from Sigma-Aldrich) deposited on glass by spray-coating. Monolayer WSe_2 and MoS_2 were grown on sapphire by chemical vapor deposition (CVD) (from 6Carbon Technology).

The structural properties of the studied samples were evaluated by scanning electron microscopy (SEM) using an FEI Nova Nano 630 apparatus as well as by transmission electron microscopy (TEM) and scanning transmission electron microscopy (STEM), while a Titan Themis Z (40−300) Thermo Fisher TEM was utilized for high-resolution STEM (HR-STEM), and high-resolution X-ray diffraction (XRD) measurements were performed on a Bruker D8 Discover apparatus with Cu Kα and λ = 1.5406 Å. For grazing incidence X-ray diffraction (GIXRD) measurements, we used a Bruker D8 Discover X-ray diffractometer equipped with a Göbel mirror and a Ge (022) monochromator using Cu Kα1 radiation (λ = 1.5406 Å) and a 0.5° incident angle to measure NWs only. Micro-Raman spectroscopy was performed using a Horiba LabRAM Aramis Raman spectrometer attached to a charge-coupled device (CCD) camera (employing the 473 nm excitation wavelength), while a 15× objective was used to focus the excitation light. In addition, energy-dispersive X-ray (EDX) spectroscopy was performed in the TEM apparatus to determine the NW composition, while TEM lamellae were prepared by an FEI Quanta 3D focused ion beam (FIB)-SEM. The room-temperature (RT) microphotoluminescence (μ-PL) and temperature-dependent PL (TDPL) measurements were carried out using a 325 nm continuous-wave He−Cd laser, while an Andor spectrograph connected to a CCD camera was used to collect the data. Power-dependent PL (PDPL) measurements at 10 K and RT (290 K) were performed by a 266 nm Teem Photonics SNU-20F-10x laser, whereby the PL signal was detected by a highly sensitive QE Pro spectrometer. We used a closed-cycle cryostat for TDPL measurements. Finally, RT cathodoluminescence (CL) hyperspectral schematic imaging was carried out using a custom-built acquisition system in an SEM, at 5 kV, while adopting an acquisition time of 100 ms/pixel.

3. RESULTS AND DISCUSSION

3.1. GaN Growth on a Wide Range of Substrates. As a part of this work, we developed a strategy for growing vertical GaN NWs on bulk and 2D substrates (exhibiting different optical and electrical properties as well as a varying degree of lattice mismatch with GaN (Table S1)) simultaneously located in the same chamber using identical conditions. Prior to commencing the growth, the PLD parameters were optimized (P_{N_2} = 150−250 mTorr; 0.95−1.05 J cm^{-2} beam fluence; d = 8.5−9 cm; and T = 850 °C, with a minimum of 40,000 laser pulses with a10 Hz laser repetition rate), as shown in the SEM images depicted in Figure 1a−h. To determine the most optimal growth conditions, we performed micro-PL, XRD, and SEM on the obtained samples after each growth run and adjusted the conditions accordingly. For this purpose, we used a commercial oxygen-doped GaN target and established the secondary-ion mass spectrometry (SIMS) profile as a function of depth (as Figure S1 confirms the presence of oxygen in the GaN target).

Figure 1a−h shows the SEM images of vertically aligned self-assembled GaN NWs grown directly and simultaneously on a wide range of bulk (Si, sapphire, GaN, and β-Ga_2O_3) and 2D (MXene, graphene, MoS_2, and WSe_2) substrates, respectively, using the proposed one-step growth method (i.e., without the need for a catalyst or a prebuffer layer). As can be seen from Figure 1i,j, depicting cross-sectional SEM images of NWs grown on Si and (−201) β-Ga_2O_3, respectively, different NW dimensions (length in the ∼1.5 ± 0.14 to ∼3.5 ± 0.17 μm range and ∼150 ± 5 to ∼200 ± 6 nm diameter) were produced by varying the number of laser pulses. Figure 1k shows that the NW length and diameter increased with the number of pulses, revealing a significant dependence. For example, under identical conditions (at 850 °C, 100,000 pulses, 200 mTorr, 100 mJ, and 9 cm target−substrate distance), the length of GaN NWs varied from ∼1.3 ± 0.14 to ∼1.5 ± 0.15 μm, whereas the average diameter and density were estimated to be ∼150 ± 5 and ∼3.9 ± 0.2 × 10^9 cm^{-2}, respectively. These results indicate that the NWs of similar quality can be grown regardless of the substrate crystallinity and orientation or its lattice mismatch with GaN, allowing this strategy to be applied to both common (including GaN) and emerging (such as Ga_2O_3 and monolayer 2D TMD) substrates without changing the growth conditions.

To further study the effect of the substrate employed on the NW quality and examine the NW crystallinity, GIXRD measurements were carried out on NWs grown simultaneously on different substrates. This strategy was adopted, as GIXRD scanning allows for an accurate NW quality evaluation as it isolates the signal produced by NWs from that yielded by other layers. It is thus superior to standard 2θ (Figure S2a) or rocking curve scans that incorporate signals generated from all sample layers. GIXRD scans shown in Figure 1l show that a single peak at 34.6° that corresponds to the (002) GaN plane was obtained for all NW samples (note that the minor peaks were produced by the background radiation noise). Moreover, the calculated c-parameter (0.518 ± 0.002 nm) agrees well with a typical strain-free GaN lattice parameter value.[22] This finding demonstrates that all NWs grown on different substrates have a single-crystalline hexagonal wurtzite structure, with an identical full width at half-maximum (fwhm) of ∼0.23 ± 0.005°. This fwhm value is comparable to that obtained for NWs using molecular beam epitaxy (MBE) and metal organic chemical vapor deposition (MOCVD) growth methods, indicating high crystal quality.[23,24] The XRD-2θ scans of all samples shown in Figure S2a reveal the dominance of the (002) plane peak at 34.6°. For all samples, minor XRD peaks of low intensity at 32.6, 36.9, 57.8, and 63.5° were observed and were assigned to the (100), (101), (110), and (103) GaN planes, respectively, based on the International Centre for Diffraction Data (ICDD) 50-0792. As will be shown later, these minor peaks are produced by the polycrystalline (poly-GaN) layer formed between the NWs and the substrates.

For 2D monolayer substrates, micro-Raman measurements were performed to examine the effect of growth conditions on

https://doi.org/10.1021/acsomega.3c06302
ACS Omega 2023, 8, 46804−46815

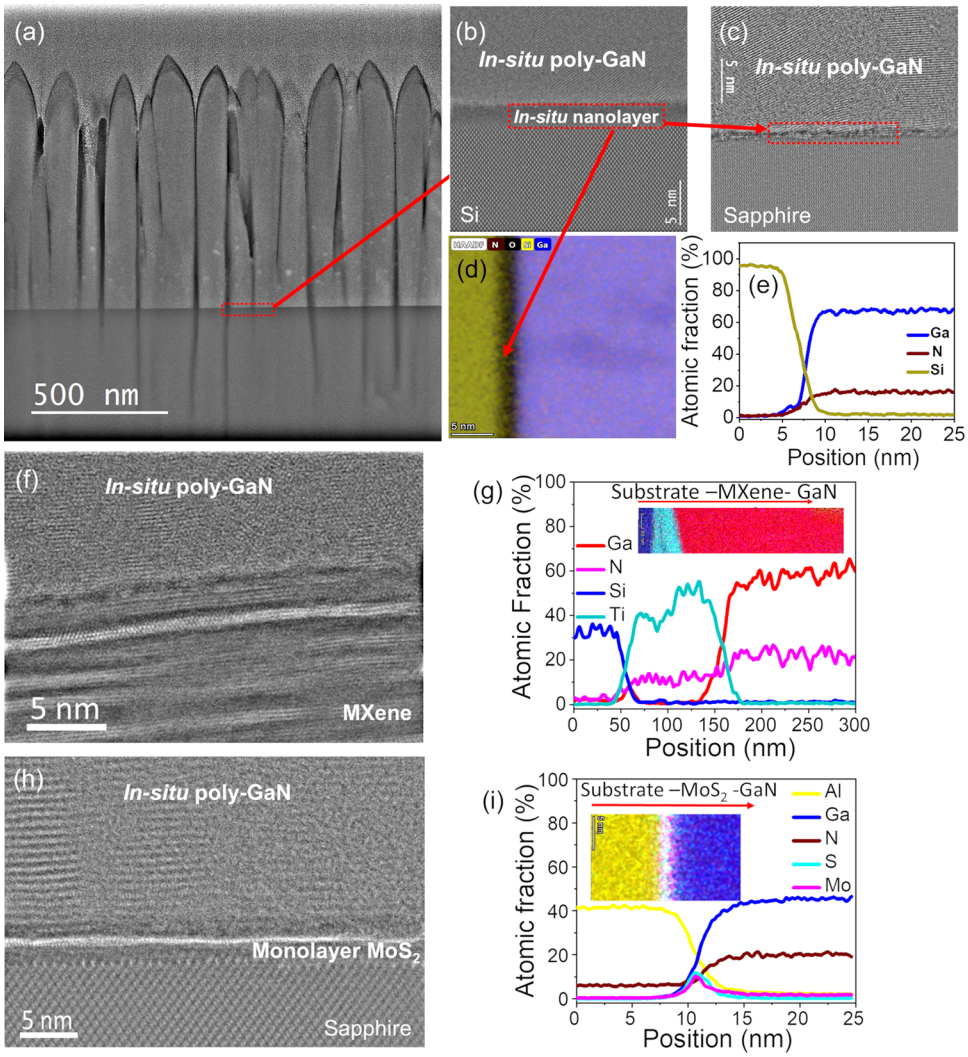

Figure 2. (a) STEM images of the GaN NWs. HR-STEM images of the poly-GaN layer on (b) Si and (c) c-sapphire substrates. The dotted red rectangular border demarcates the *in situ* nanolayer at the interface between poly-GaN and substrates. (d) The corresponding EDX map and (e) its profile. HR-STEM images and its elemental profiles of the GaN–substrate interface grown on (f, g) MXene and the corresponding EDX profile (the inset shows the EDX map) and (h, i) MoS_2 substrates and the corresponding EDX profile (the inset shows the EDX map).

the properties of monolayer 2D substrates (Figure S2b). No significant differences were observed in the Raman spectra of the 2D substrates obtained after NW growth, demonstrating that their initial crystallinity was well maintained during PLD growth. Compared to the peak position prior to growth (as evident from Figure S3 depicting the Raman spectra of bare 2D MoS_2 and WSe_2 monolayers), a slight shift was observed after NW growth and was attributed to the bond strain due to the epitaxial NW growth.[25−27] Furthermore, none of the Raman and XRD spectra provided evidence of secondary phases (e.g., Ga oxynitride), as shown in Figure S2.

To examine the possibility of obtaining GaN NWs on large wafer substrates, GaN NWs were grown on a 4 in. Si substrate. The SEM images presented in Figure S4a–c reveal that the NWs at the 4″ Si wafer edge exhibited a slight tilt compared to those located in the center. The height of NWs remained roughly the same up to the 2 in. diameter, as shown in the SEM images illustrated in Figure S4e,f. However, μ-PL spectra collected from areas across the whole wafer (Figure S4d) contain a strong UV GaN near band edge (NBE) peak. On the other hand, the much weaker defect yellow luminescence (YL) in all spectra indicates that good structural quality is maintained across the entire wafer, suggesting that our method is suitable for large-scale applications.

3.2. HR-STEM Characterizations at the GaN–Substrate Interface. *3.2.1. In Situ Polycrystalline GaN Layer.* To gain insight into the NW growth mechanism, we carried out extensive HR-STEM and EDX measurements for elemental mapping of GaN NWs grown on all substrates. The STEM image in Figure 2a shows the vertical self-assembled GaN NW structure. (Note that vertical lines that are visible across the entire substrate are attributed to the ion beam penetration between NWs during the FIB lamella preparation.)

Figure 2b–i shows the cross-sectional HR-STEM images and the corresponding EDX maps and profiles of the area near the substrate for samples grown on Si, sapphire, 2D MXene, and single-layer TMD (e.g., MoS_2) substrates, respectively. The HR-STEM images reveal that an *in situ* poly-GaN layer was formed below GaN NWs, during growth on all bulk and 2D substrates, as shown in Figure 2b,c for Si and sapphire, as well as Figure 2f,h for 2D MXene and monolayer MoS_2 substrates. This poly-GaN layer consists of many single-

https://doi.org/10.1021/acsomega.3c06302
ACS Omega 2023, 8, 46804−46815

crystalline nanograins with different orientations, which is in line with the different minor GaN peaks observed in the XRD-2θ scans (Figure S2a). Similar results were obtained for all other substrates, as shown in the HR-STEM images illustrated in Figure 3a–d. The fast Fourier transform (FFT) patterns

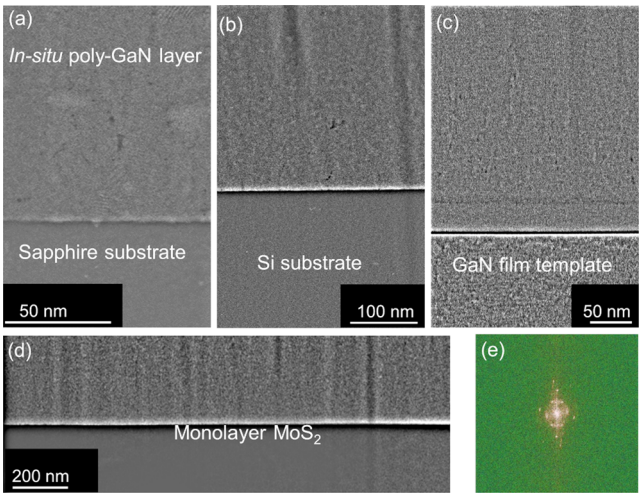

Figure 3. STEM images of the interface between the poly-GaN layer and different substrates for samples grown on a (a) sapphire, (b) Si, (c) p-GaN film, and (d) MoS_2 monolayer. Note that the black spots and lines are due to the FIB effect. (e) FFT patterns of the poly-GaN layer.

depicted in Figure 3e further indicate that the ring diffraction shape arises due to the different nanograin orientations in the poly-GaN area.

The STEM images of a wider area illustrated in Figure S5 indicate that, under the PLD conditions used in this work, the poly-GaN layer thickness remains at ∼300 nm for all samples grown on bulk and 2D substrates. As expected, comparable grain sizes (in the ∼8 to ∼15 nm range) are obtained in samples grown on different substrates.[28] Therefore, no obvious correlation between the substrate type and the poly-GaN layer thickness and grain size or NW structure is observed as all substrates were simultaneously exposed to identical PLD conditions. In addition, as shown in the HR-STEM images illustrated in Figures 2 and 3, no evidence was found of TD propagation from the substrate interface to the poly-GaN layer due to the fact that the random misorientation between the nanograins in the poly-GaN layer is large enough to stop TD propagation, as Burgers vector is different for nanograins with different orientations.[29] Similarly, owing to the effect of different nanograin orientations, no crystallographic relationship between the poly-GaN layer and the substrate can be established.[30,31]

The HR-STEM images taken near the substrate shown in Figures 2b,c and 3 reveal that a homogeneous *in situ* nanolayer of uniform ∼2 nm thickness was formed above the substrate during PLD growth using the oxygen-doped GaN target as oxygen migrates into the interface with the substrates as a result of limited solubility.[20,21,32]

3.2.2. Single-Crystalline Nature of GaN NWs. As shown in Figure 4a–h, HR-STEM analyses demonstrated the high-quality and single-crystalline structure of vertically aligned wurtzite GaN NWs for all samples grown on all bulk and 2D substrates, which is in line with the GIXRD results. The single-crystalline wurtzite structure of NWs along the *c*-direction was further demonstrated by selected area electron diffraction (SAED) and FFT patterns obtained from different NW areas, as indicated in Figure 4i.

To explore the process underpinning the transformation from polycrystallinity to single crystallinity in our samples, HR-STEM measurements were performed at different locations situated progressively further away (vertically) from the substrate interface, as shown in Figure 4j,k. The HR-STEM images provided in Figure 4k—corresponding to the segments surrounded by the yellow dotted line in Figure 4j—confirm the crystalline nature of the depicted areas. These HR-STEM images also reveal that the polycrystalline characteristics diminish as the poly-GaN thickness increases. Figure 4k further shows that, at a >300 nm vertical distance from the substrate (GaN NW bottom), the structure becomes single-crystalline along the *c*-direction and is retained throughout the entire NW structure, as confirmed by images shown in Figure 4a–h.

The EDX maps and profiles presented in Figure 4l measured from the substrate to the top of NWs indicate that, while oxygen concentration is the greatest in the poly-GaN/substrate interface, it declines to <5 atom % when the distance from the substrate exceeds 300 nm (i.e., at the end of the poly-GaN layer at which point the single-crystalline structure is initiated) and remains constant across the entire NW length. Figure S6 shows a similar behavior for all samples. Due to the low solubility of oxygen in crystalline GaN,[35] oxygen accumulates in the poly-GaN layer, while a small amount remains in the NWs, as shown by EDX profiles presented in Figure 4l.

3.3. In-Depth Investigation of the NW Growth Mechanism. Our growth method is denoted as a "one-step growth" as it does not require any changes to the temperature, pressure, or layer components. Similarly, it does not involve the use of a prebuffer layer or seeding and does not require an increase in the N_2 supply during growth, while the NWs are grown simultaneously on different substrates that have similar quality and properties. When PLD is employed, the nucleation surface energy depends on the energy of the charged species landed on the substrate,[28] which can be modified to control the material structure.[20,21,36] This species energy depends on the initial energy of the charged species in the plume emerging from the target surface, the distance between the target and the substrate, the growth temperature, and the nitrogen pressure. When the kinetic energy (E) of the charged species arriving at the substrate surface is sufficiently low, it allows NW formation on the poly-GaN layer without catalysis or seeding.[33,37] The relatively high PN_2 (≥150 mTorr) and/or relatively low E_0 of the ablated species can reduce the E value due to high species scattering as a result of a large number of collisions with nitrogen molecules, leading to NW nucleation.[33,37] As the effect of species kinetic energy in PLD is analogous to that of impinging the Ga flux on the substrate in MBE, it has a similar impact on the NW growth.[38] Therefore, the effect of the growth parameters (temperature, laser power, pressure, and number of pulses) on NW characteristics is significant, as shown in Figures S7–S10, respectively. The optimized temperature (850 °C) is similar to that used in MBE.[28,39] The μ-PL spectra of optimized NWs (as illustrated in Figure S11) showed typical GaN emission,[40,41] with a UV NBE emission quality that is superior to those produced under other PLD conditions.

As shown in Figure 4k, the grain size increases until a single-crystalline structure is attained and NW formation is initiated,

https://doi.org/10.1021/acsomega.3c06302
ACS Omega 2023, 8, 46804−46815

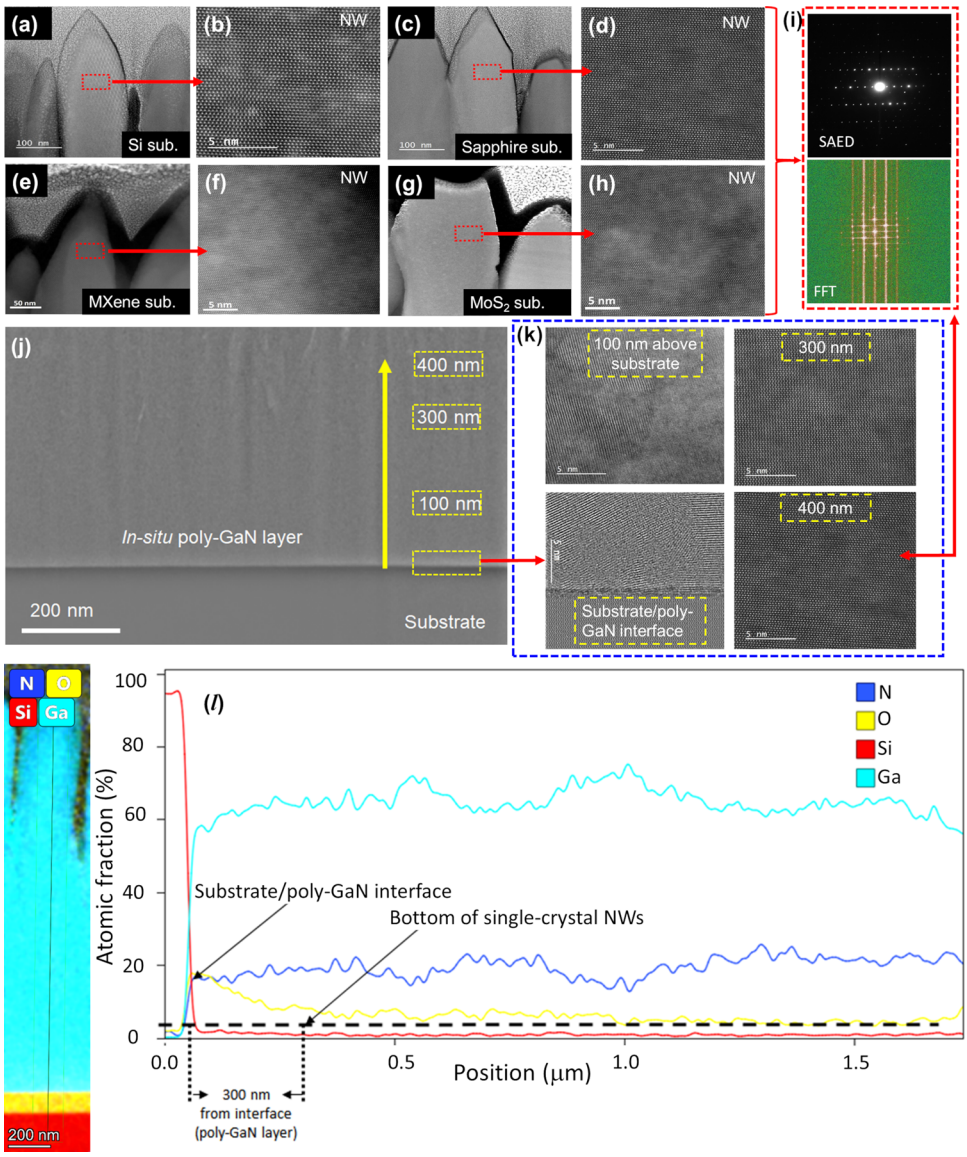

Figure 4. STEM images of single-crystal GaN NWs grown on different substrates: (a) on Si and (b) the corresponding HR-STEM image; (c) on c-sapphire (d) and the corresponding HR-STEM image; (e) MXene (f) and the corresponding HR-STEM image; and (g) MoS_2 (h) and the corresponding HR-STEM image. (i) The corresponding SAED and FFT patterns of the single-crystalline NWs. (j) STEM image of a full poly-GaN layer and (k) the dotted blue box: the corresponding HR-STEM images taken at the interface (the bottom left panel) and at 100 nm (top left), 300 nm (top right), and 400 nm (bottom right) above the interface. (l) EDX elemental map extending from the substrate to the top of the NW (left panel) and the corresponding EDX profile (right panel).

i.e., at 300 nm above the substrate, while Figure S12 further confirms that the grain size increases as the poly-GaN layer thickness increases until the single-crystalline structure is obtained in the bottom of the NWs. This finding is ascribed to different factors, including the increase in the layer thickness,[42,43] the time required for deposition,[44,45] and the decrease in the dopant (in this case oxygen) concentration.[46] Previously reported findings indicate that, as the temperature gradient occurs as the polylayer thickness increases, the grain size becomes larger.[47] Previously, the transformation from polycrystalline to the single-crystal phase was observed and has been explained from the classic theory of the grain boundary migration perspective, indicating that the formation energy along the growth direction plays a role in this process.[47,48] Thus, in our case, as the formation energy of GaN along the *c*-axis is much lower than in other directions,[49] they are aligned along the *c*-direction only while progressive elimination of different orientation grains occurs during growth, resulting in a single-crystalline phase (a schematic illustration of this growth mechanism is shown in Figure S14). Similar explanations for the phase transformation have been offered in the pertinent literature for different materials.[47−49] Such a growth mechanism of single-crystalline GaN NWs is similar to the growth features observed in the columnar growth of NWs typically seen in MBE.[38,50,51]

To understand the growth mechanism, we study the strain behavior by evaluating the lattice parameters from the substrate/poly-GaN interface to the NW top using advanced HR-STEM analyses and the corresponding FFT and inverse FFT (IFFT) patterns. Such analyses assist in understanding the role of strain in single-crystalline NW formation. Figure 5a depicts the STEM image of the NWs from which all HR-

https://doi.org/10.1021/acsomega.3c06302
ACS Omega 2023, 8, 46804−46815

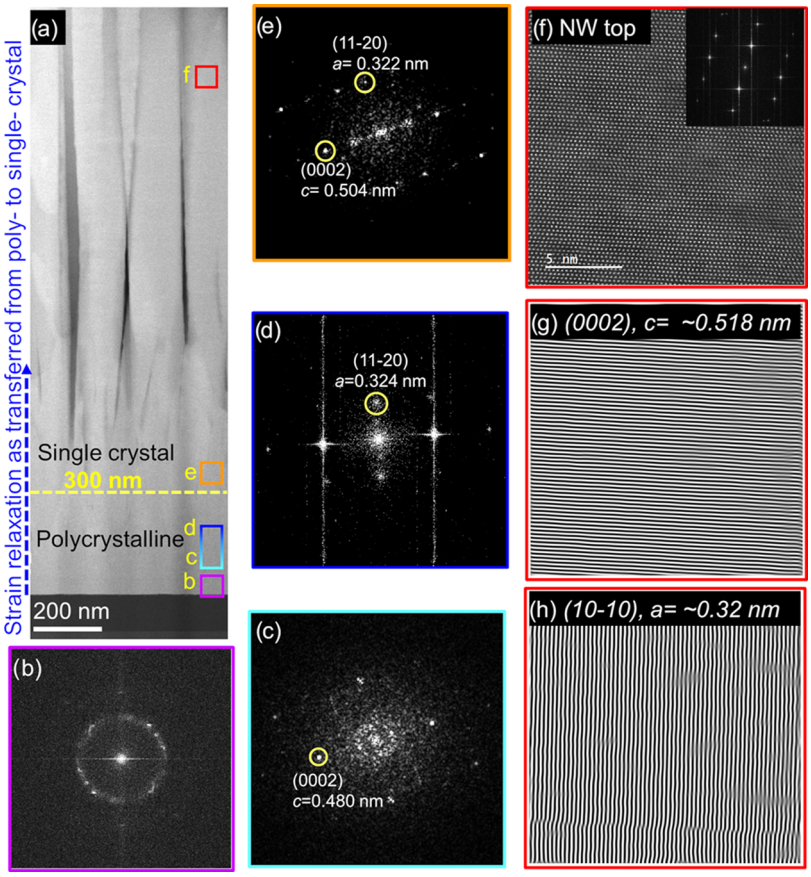

Figure 5. (a) STEM image of NWs including the poly-GaN layer. The yellow dotted line indicates the end of the polycrystalline layer (at 300 nm). The vertical dotted blue arrow indicates the strain relaxation direction from the substrate to NWs. FFT patterns are taken from HR-STEM and HR-TEM images acquired at (b) the interface between the substrate and GaN (area demarcated by the purple square in panel (a)); (c) 50 nm (area demarcated by the cyan square), (d) 200 nm (area demarcated by the blue square), and (e) above 300 nm (area demarcated by the orange square). (f) HR-STEM and the corresponding FFT patterns (inset) taken from the top of NW (area demarcated by the red square), as well as the corresponding IFFT patterns for (g) the (0002) plane and (h) the (10−10) plane where the lattice parameters are estimated.

STEM images were taken (Figure S13). The corresponding FFT patterns shown in Figure 5b−f reveal that the lattice parameter values change as the vertical distance from the substrate to the NW increases. The yellow dotted line in Figure 5a demarcates the position at which the poly-GaN layer terminates (at a 300 nm height from the substrate).

Figure 5b shows the FFT taken at the substrate/poly-GaN interface, and the ring diffraction shape is obtained due to a roughly amorphous structure. The image shown in Figure 5c illustrates the FFT patterns obtained from HR-STEM images in Figure S13 (taken at an ∼100 nm height from the substrate), where a *c*-parameter of 0.48 nm is obtained. However, different grains with different orientations are characterized by the *a*-parameter of 0.33 nm, as evident from the FFT patterns illustrated in Figure S13a, demonstrating a well-strained poly-GaN layer (note that, in the poly-GaN layer, we can observe either the *a*- or *c*-direction depending on the grain orientation). As shown in FFT patterns in Figure 5d taken from HR-STEM in Figure S13b, at a 200 nm height from the substrate, the layer starts to relax, as indicated by the *a*-parameter of 0.324 nm. Moreover, IFFT and FFT patterns obtained at 300 nm from the substrate shown in Figure S13c demonstrate that when grains become larger, the *a*-parameter relaxes further, taking the value of 0.323 nm. In previous studies, grain boundaries were found to be a source of intrinsic stress in polycrystalline materials[31] as the interatomic forces at the grain boundaries tend to close any existing gaps due to which the neighboring nanograins are strained.[30] However, as the grain size increases, strain relaxation occurs,[52] which is in line with our findings.

At a 400 nm height from the substrate (i.e., above the poly-GaN layer), the single-crystalline structure commences, allowing the FFT and IFFT patterns to be resolved to the *c*-direction and *a*-direction, as shown in Figures 5e (extracted from the HR-STEM images shown in Figure S13d). At this point, the strain along the *c*-direction starts relaxing (c = 0.504 nm), while a slight relaxation is also observed in the *a*-parameter (a = 0.322 nm). The analyses of FFT and IFFT patterns—depicted in the inset of Figure 5f−h—near the top of the NWs (Figure 5f) confirm a fully relaxed GaN structure, and the resulting c = 0.518 nm and a = 0.320 nm values are comparable to those of free-strained GaN while concurring with our XRD and GIXRD results.

HR-STEM analyses yielded similar findings for NWs grown on different substrates, indicating that the NW nucleation mode, which is correlated to the landed species energy E in PLD growth, is controlled by the built-in stress. Here, the strained layer (*in situ* poly-GaN) is formed first. Then, as the material continuously relaxes owing to lattice distortion in the growth direction, the growth mode transforms from the layer-by-layer mode to the 3D nucleation mode, resulting in the emergence of self-assembled NWs.[33] In columnar NW growth,

https://doi.org/10.1021/acsomega.3c06302
ACS Omega 2023, 8, 46804−46815

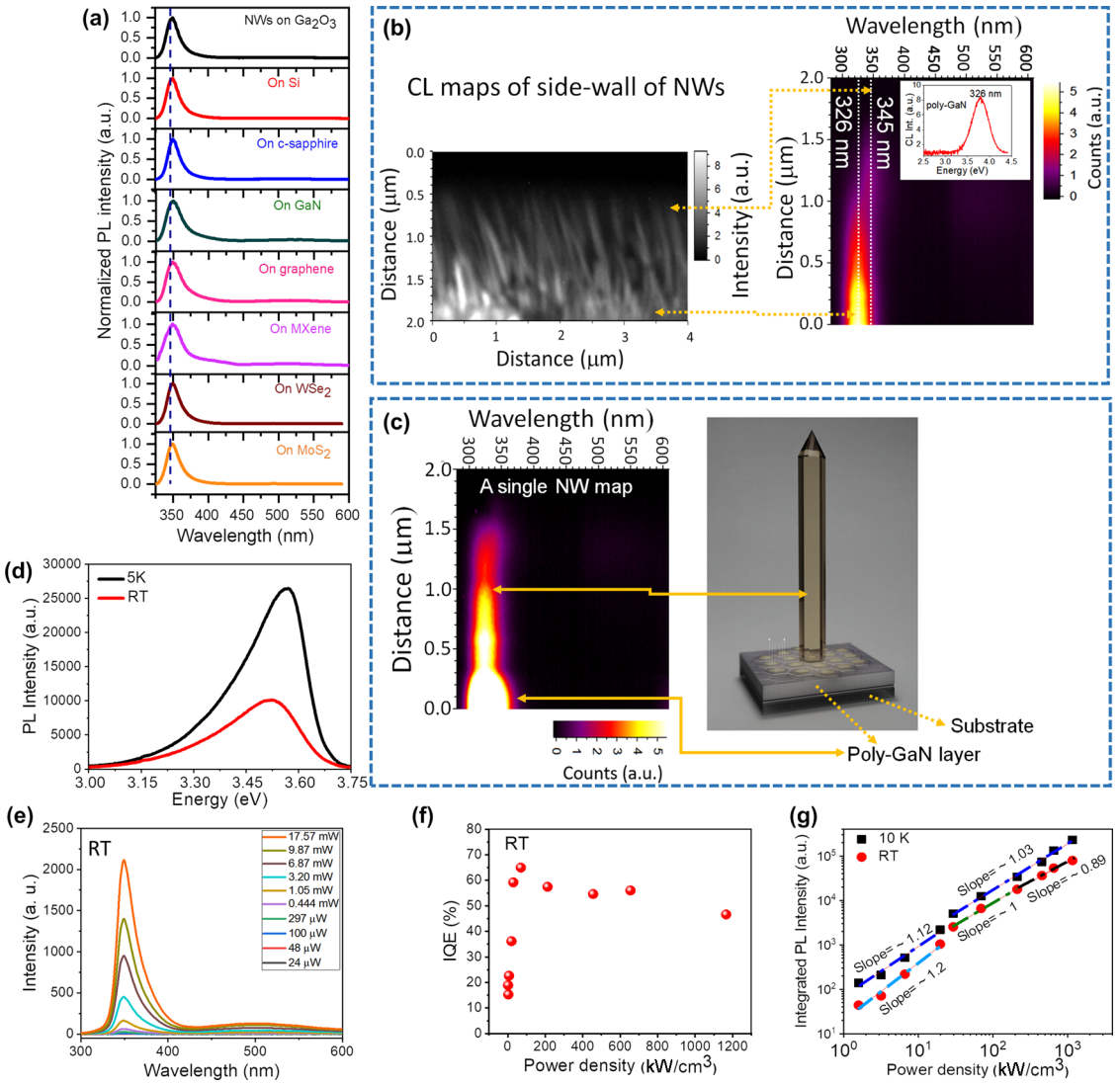

Figure 6. (a) μ-PL spectra pertaining to GaN NWs grown on all substrates. (b) The left panel: the cross-sectional CL map of the NW sample from the poly-GaN layer to the NW top; and the right panel: the corresponding RT integrated CL spectral map. (c) The left panel: RT CL spectral map of a single NW taken from the poly-GaN layer to the NW top; and the right panel: its schematic diagram. (d) Temperature-dependent PL spectra of GaN NWs at RT and 5 K. (e) Power-dependent PL spectra at RT. (f) IQE as a function of the power density at RT. (g) Log–log integrated RT PL intensity vs the laser excitation density.

relaxation was found to be a necessary condition for the self-induced formation of NW nuclei, as the initial deposition of a 2D wetting layer is followed by the nucleation of almost fully relaxed NW nuclei.[53] Similar mechanisms can also be considered for the NW growth by PLD in this study. Thus, the poly-GaN layer may assist in forming suitable nucleation centers for NW formation similar to that observed in the Stranski–Krastanov (film + nanostructure) growth mode (as shown in the schematic diagram in Figure S14). In addition, based on the surface energy theory,[33,34] the interface oxygen-rich *in situ* nanolayer might impact growth by affecting the NW nucleation process. Such a process can eliminate the substrate dependence.[53]

3.4. NW Quality Evaluation through Optical Analyses.

3.4.1. Emission Properties. To further confirm the NW quality, we conducted μ-PL as well as TDPL and PDPL measurements as they are powerful, commonly used tools for evaluating the material quality. Figure 6a shows the RT μ-PL spectra, revealing a dominant UV NBE emission centered at ~3.55 eV for NWs grown on all substrates, along with a weak defect YL band emission (the log-scales of PL spectra of all samples are shown in Figure S15 to confirm the dominant band edge emission), which is a typical GaN emission as such a weak YL confirms its good optical quality.[41,54] This result is also in line with the STEM and GIXRD results, demonstrating the success of our growth method. No discernible change in the PL spectra was observed for the NW grown on different substrates.

To investigate the PL peak broadening, the emission originating from different parts of the samples was studied by RT CL hyperspectral imaging, allowing the emissions from the poly-GaN layer and NW regions to be spatially resolved. The CL maps illustrated in the left panel of Figure 6b were acquired from a cross-sectional SEM image of the GaN NW sample taken from the top to the bottom of the sample. The 2D integrated CL spectrum provided in the right panel of Figure 6b reveals two peaks centered at ~345 nm (~3.59 eV) and ~326 nm (~3.8 eV), which are emitted from the NWs and

https://doi.org/10.1021/acsomega.3c06302
ACS Omega 2023, 8, 46804−46815

poly-GaN, respectively. The NW emission peak at ∼3.59 eV is closer to the PL peak, confirming that the dominant emission is generated from the NWs. The CL spectrum of poly-GaN at 3.8 eV shown in the inset of Figure 6b indicates that its NBE peak is blue-shifted and much broader. Figure 6c shows the CL map of a single NW taken by traversing from the poly-GaN layer to the top of the NW, further confirming the dominant NBE of NW, as well as the broader emission of the poly-GaN compared to that of NW.

There are several causes of such PL emission broadening, one of which can be the residual strain distribution[55,56] in the poly-GaN layer and NWs as different nanograin sizes would result in variation in strain in the poly-GaN layer. In addition, the presence of impurities,[57] including oxygen in GaN,[58] generally causes broadening of the PL band edge emission. Notably, Okada et al.[59] indicated that when oxygen (in concentrations ranging from 7×10^{16} to $1 \times 10^{17}/cm^3$) was introduced in the InGaN active layer (without Si doping), the light output power of the LED can be improved, suggesting that the presence of oxygen may improve the optical emission in NWs. However, a detailed study of this phenomenon is beyond the scope of this work. Furthermore, Figure S16 shows the sharp absorption edge of GaN NWs with an RT band gap at 3.56 eV,[60] which is in line with the single-crystalline GaN value, and the absorption tail is most probably due to the poly-GaN layer.

3.4.2. Internal Quantum Efficiency Analysis and Dominant Radiative Recombination. To provide additional evidence of high NW quality, optical efficiency (mainly IQE) was calculated through both TDPL[61−63] and PDPL methods. Figure 6d shows that the NBE emission is intense at both RT and 5 K. Moreover, the ratio of PL intensity at 5 K to that at RT was ∼44% for the sample grown on Si (Figure 6d), and it ranged from ∼40% to 45% for all samples, suggesting single-crystalline NWs of high optical quality.[61−63]

The high IQE of GaN NWs was also validated by calculating its value for the sample grown on Si, using the Shockley−Read−Hall (SRH) method based on PDPL measurements, which is considered an accurate and reliable method for calculating the IQE at RT.[64,65] For this purpose, the PDPL spectra shown in Figure 6e were obtained under different injected laser powers. The IQE was calculated by applying the ABC model to the PDPL data, using the total recombination rate equation[28,66]

$$G = An + Bn^2 + Cn^3 \quad (1)$$

where An represents the SRH nonradiative recombination rate, Bn^2 denotes the radiative recombination rate, and Cn^3 is the carrier Auger-like nonradiative recombination rate. As can be seen from eq 1, the three regimes can be represented via the relationship between the injected current density (G) and carrier concentration (I), whereby $I_{PL} \propto G^k$, as defined by the following relation[67,68]

$$G_{opt} = Q_1\sqrt{I_{PL}} + Q_2 I_{PL} + Q_3 (I_{PL})^{3/2} \quad (2)$$

where Q_1, Q_2, and Q_3 indicate the fitting parameters explained in terms of A, B, and C. For the nonradiative SRH recombination regime, $k = 2$ at a low carrier injection density. At high carrier concentration, $k = 2/3$ or 0.66 denotes the Auger recombination regime, whereas $k = 1$ holds when the total radiative recombination regime is applied.[68]

Consequently, the IQE at steady state can be expressed as[67,68]

$$\eta_{IQE} = \frac{Bn^2}{G_{opt}} = \frac{Q_2 I_{PL}}{G_{opt}} \quad (3)$$

where Q_2 is a constant (the detailed calculation method was explained elsewhere).[28,66−69] The power-dependent IQE as a function of the injected carrier density at RT is shown in Figure 6f, indicating that the IQE increases rapidly with excitation energy density. This trend is attributed to the saturation of the nonradiative recombination centers by generated carriers,[67] whereby its maximum value (65%) is achieved at ∼70 kW/cm^3, demonstrating a significant predominance of radiative recombination. At higher excitation energy densities, the IQE starts to decline, reaching ∼47% at 1.2×10^3 kW/cm^3, which is in line with the IQE values yielded by TDPL. Such an IQE value is considered high for GaN UV emission and is comparable to that obtained from high-quality NWs grown by MBE.[61−63] The droop regime that follows a convex curve was attributed to the dominant effect of defect-related nonradiative recombination through the SRH process, whereas the droop that follows the concave regime was ascribed to the carrier overflow mechanism[66,70] Thus, the concave IQE droop behavior of these NWs further confirms the dominant radiative recombination process even after the droop.

To gain further insight into the radiative recombination contribution and identify the reasons behind the droop, we plotted log (I_{PL}) as a function of log (G_{opt}) (power density) at RT and 10 K. Figure 6g shows that $k \sim 1.2$ is obtained at RT under a low excitation power density, further confirming the significant contribution of the radiative recombination accompanied by negligible nonradiative recombination. On the other hand, at the higher end of the IQE range, i.e., at ≥30 kW/cm^3 before the onset of the droop regime where $k = 1$ is obtained—high excitation power density leads to the saturation of nonradiative centers, showing that the radiative recombination process fully governs the observed emission. However, in the efficiency droop range, the slope of ∼0.89 is obtained, suggesting that dominant radiative recombination is accompanied by a minor Auger recombination contribution, which is likely the main reason behind the slight IQE droop. At low temperature (10 K), the k is in the 1−1.1 range, indicating that radiative recombination predominates in both low and high excitation densities, where the IQE value at 10 K is 100% and is accompanied by a slight droop (IQE = 92%) in the high excitation region. These results provide ample evidence in support of the high NW quality and suggest that our method can be potentially used in a wide range of applications.

4. CONCLUSIONS

We have established a successful growth strategy for obtaining high-quality self-assembled GaN NWs simultaneously on any 2D TMD or bulk substrates placed in the same chamber and thus subjected to identical conditions. As no metal catalyst, prenucleation, or buffer layer was required, this facile and cost-effective method can be adopted for growth on a wide range of emerging substrates, such as Ga_2O_3 monolayer 2D TMD substrates, as well as lattice-matched substrates (including GaN) without seeding or the use of additional buffer layer. Our extensive analyses indicate that the growth mechanism progresses from the poly-GaN layer toward single-crystalline

https://doi.org/10.1021/acsomega.3c06302
ACS Omega 2023, 8, 46804−46815

NWs, while the advanced optical analyses and carrier dynamics measurements carried out as a part of this work confirm the good optical properties and high optical efficiency of the obtained NWs. As this growth strategy allowed the simultaneous NW growth on different substrates without the need for modifying the growth conditions, it can be generalized for developing III-nitride devices for large-scale applications, as it can eliminate the need for the lift-off and device transfer, which are highly complex processes. Moreover, this single-step growth method can be applied using other techniques, such as sputtering or MBE, by controlling the energy with which the species lend to the substrate.

■ ASSOCIATED CONTENT

Supporting Information

The Supporting Information is available free of charge at https://pubs.acs.org/doi/10.1021/acsomega.3c06302.

Substrate properties and their lattice mismatch with GaN; secondary-ion mass spectrometry (SIMS) for evaluation of oxygen dopants in the GaN target; 2θ-XRD scans and Raman measurements for all samples; SEM images and μ-PL spectra were acquired at different positions across the 4″ substrate; STEM and HR-STEM images of NWs grown on different substrates at the same time; the profile of the chemical distribution across the sample; the strain effect on lattice parameter values of the poly-GaN as the thickness increases above the substrate and the grain size increases with thickness; and the effect of laser energy, pressure, temperature, and number of laser pulses; the schematic diagram of the growth mechanism; HR-STEM and the corresponding FFT patterns; the PL and absorption spectra of NW samples (PDF)

■ AUTHOR INFORMATION

Corresponding Author

Iman S. Roqan − *Physical Science and Engineering Division, King Abdullah University of Science and Technology (KAUST), Thuwal 23955, Saudi Arabia;* orcid.org/0000-0001-7442-4330; Email: iman.roqan@kaust.edu.sa

Authors

Dhaifallah Almalawi − *Physical Science and Engineering Division, King Abdullah University of Science and Technology (KAUST), Thuwal 23955, Saudi Arabia; Department of Physics, College of Science, Taif University, Taif 21944, Saudi Arabia*

Sergei Lopatin − *Imaging and Characterization Core Laboratory, King Abdullah University of Science and Technology (KAUST), Thuwal 23955, Saudi Arabia*

Paul R. Edwards − *Department of Physics, SUPA, University of Strathclyde, Glasgow G4 0NG, United Kingdom;* orcid.org/0000-0001-7671-7698

Bin Xin − *Physical Science and Engineering Division, King Abdullah University of Science and Technology (KAUST), Thuwal 23955, Saudi Arabia*

Ram C. Subedi − *Photonics Laboratory, Division of Computer, Electrical and Mathematical Sciences and Engineering, King Abdullah University of Science and Technology (KAUST), Thuwal 23955, Saudi Arabia;* orcid.org/0000-0003-2818-1352

Mohammed A. Najmi − *Division of Computer, Electrical and Mathematical Sciences and Engineering, King Abdullah University of Science and Technology (KAUST), Thuwal 23955, Saudi Arabia;* orcid.org/0000-0002-3214-6683

Fatimah Alreshidi − *Physical Science and Engineering Division, King Abdullah University of Science and Technology (KAUST), Thuwal 23955, Saudi Arabia*

Alessandro Genovese − *Imaging and Characterization Core Laboratory, King Abdullah University of Science and Technology (KAUST), Thuwal 23955, Saudi Arabia*

Daisuke Iida − *Division of Computer, Electrical and Mathematical Sciences and Engineering, King Abdullah University of Science and Technology (KAUST), Thuwal 23955, Saudi Arabia*

Nimer Wehbe − *Imaging and Characterization Core Laboratory, King Abdullah University of Science and Technology (KAUST), Thuwal 23955, Saudi Arabia*

Boon S. Ooi − *Photonics Laboratory, Division of Computer, Electrical and Mathematical Sciences and Engineering, King Abdullah University of Science and Technology (KAUST), Thuwal 23955, Saudi Arabia*

Kazuhiro Ohkawa − *Division of Computer, Electrical and Mathematical Sciences and Engineering, King Abdullah University of Science and Technology (KAUST), Thuwal 23955, Saudi Arabia;* orcid.org/0000-0002-8728-3503

Robert W. Martin − *Department of Physics, SUPA, University of Strathclyde, Glasgow G4 0NG, United Kingdom;* orcid.org/0000-0002-6119-764X

Complete contact information is available at: https://pubs.acs.org/10.1021/acsomega.3c06302

Author Contributions

$^{\nabla}$D.A. and I.S.R. contributed equally as a first author. All authors discussed and agreed on the final version of the manuscript.

Notes

The authors declare no competing financial interest.

■ ACKNOWLEDGMENTS

I.S.R. thanks KAUST for the financial support using the base fund (BAS/1/1319-01-01). The schematic in Figure ^{6}c and TOC was created by Ivan Gromicho, Scientific Illustrator at the King Abdullah University of Science and Technology (KAUST).

■ REFERENCES

(1) Zhang, A.; Ren, F.; Anderson, T.; Abernathy, C.; Singh, R.; Holloway, P.; Pearton, S.; Palmer, D.; McGuire, G. High-power GaN electronic devices. *Crit. Rev. Solid State Mater. Sci.* **2002**, *27* (1), 1−71.

(2) Medjdoub, F., *Gallium Nitride (GaN): Physics, Devices, and Technology*. CRC Press: 2017.

(3) Li, G.; Wang, W.; Yang, W.; Lin, Y.; Wang, H.; Lin, Z.; Zhou, S. GaN-based light-emitting diodes on various substrates: a critical review. *Rep. Prog. Phys.* **2016**, *79* (5), No. 056501.

(4) Shur, M. GaN based transistors for high power applications. *Solid-State Electron.* **1998**, *42* (12), 2131−2138.

(5) Ebaid, M.; Kang, J.-H.; Ryu, S.-W. Controlled synthesis of GaN-based nanowires for photoelectrochemical water splitting applications. *Semicond. Sci. Technol.* **2017**, *32* (1), No. 013001.

(6) Acharya, A. R. Group III−nitride semiconductors: preeminent materials for modern electronic and optoelectronic applications. *Himalayan Phys.* **2015**, *5*, 22−26.

(7) Yoo, H. G.; Park, K.-I.; Koo, M.; Kim, S.; Lee, S. Y.; Lee, S. H.; Lee, K. J. Quantum Sensing and Nanophotonic Devices IX. In *Flexible*

https://doi.org/10.1021/acsomega.3c06302
ACS Omega 2023, 8, 46804−46815

GaN LED on a Polyimide Substrate for Display Applications; SPIE, 2012; pp 436−441.
(8) Kirste, R.; Rohrbaugh, N.; Bryan, I.; Bryan, Z.; Collazo, R.; Ivanisevic, A. Electronic biosensors based on III-nitride semiconductors. *Annu. Rev. Anal. Chem.* **2015**, *8*, 149−169.
(9) Haglund, Å.; Hashemi, E.; Bengtsson, J.; Gustavsson, J.; Stattin, M.; Calciati, M.; Goano, M. Progress and challenges in electrically pumped GaN-based VCSELs. *Proc. SPIE* **2016**, *9892*, 161−180, DOI: 10.1117/12.2229428.
(10) Manasreh, M. O. *III − Nitride Semiconductors: Electrical, Structural and Defects Properties*. Elsevier: Amsterdam, 2000.
(11) Liu, L.; Edgar, J. H. Substrates for gallium nitride epitaxy. *Mater. Sci. Eng. R* **2002**, *37* (3), 61−127.
(12) Suihkonen, S.; Pimputkar, S.; Sintonen, S.; Tuomisto, F. Defects in single crystalline ammonothermal gallium nitride. *Adv. Electron. Mater.* **2017**, *3* (6), No. 1600496.
(13) Guo, W.; Zhang, M.; Banerjee, A.; Bhattacharya, P. Catalyst-free InGaN/GaN nanowire light emitting diodes grown on (001) silicon by molecular beam epitaxy. *Nano Lett.* **2010**, *10* (9), 3355−3359.
(14) Hersee, S. D.; Rishinaramangalam, A. K.; Fairchild, M. N.; Zhang, L.; Varangis, P. Threading defect elimination in GaN nanowires. *J. Mater. Res.* **2011**, *26* (17), 2293.
(15) Kumaresan, V.; Largeau, L.; Madouri, A.; Glas, F.; Zhang, H.; Oehler, F.; Cavanna, A.; Babichev, A.; Travers, L.; Gogneau, N.; et al. Epitaxy of GaN nanowires on graphene. *Nano Lett.* **2016**, *16* (8), 4895−4902.
(16) Tian, H.; He, Y.; Das, P.; Cui, Z.; Shi, W.; Khanaki, A.; Lake, R. K.; Liu, J. Growth Dynamics of Millimeter-Sized Single-Crystal Hexagonal Boron Nitride Monolayers on Secondary Recrystallized Ni (100) Substrates. *Adv. Mater. Interfaces* **2019**, *6* (22), No. 1901198.
(17) Prabaswara, A.; Kim, H.; Min, J.-W.; Subedi, R. C.; Anjum, D. H.; Davaasuren, B.; Moore, K.; Conroy, M.; Mitra, S.; Roqan, I. S.; et al. Titanium Carbide MXene Nucleation Layer for Epitaxial Growth of High-Quality GaN Nanowires on Amorphous Substrates. *ACS Nano* **2020**, *14* (2), 2202−2211.
(18) Choi, J. H.; Ahn, H. Y.; Lee, Y. S.; Park, K.; Kim, T.-H.; Cho, K. S.; Baik, C. W.; Kim, S. I.; Yoo, H.; Lee, E. H.; et al. GaN light-emitting diodes on glass substrates with enhanced electroluminescence. *J. Mater. Chem.* **2012**, *22* (43), 22942−22948.
(19) Kawan, A.; Yu, S.-J.; Sung, J.-H. Study of laser lift-off process for fabrication of GaN-based 365-nm ultraviolet absorption layer removed flip chip LED. *Trans. Electr. Electron. Mater.* **2018**, *19* (3), 230−234.
(20) Alwadai, N.; Ajia, I. A.; Janjua, B.; Flemban, T. H.; Mitra, S.; Wehbe, N.; Wei, N.; Lopatin, S.; Ooi, B. S.; Roqan, I. S. Catalyst-Free Vertical ZnO-Nanotube Array Grown on p-GaN for UV-Light-Emitting Devices. *ACS Appl. Mater. Interfaces* **2019**, *11*, 27989−27996, DOI: 10.1021/acsami.9b06195.
(21) Flemban, T. H.; Singaravelu, V.; Devi, A. A. S.; Roqan, I. S. Homogeneous vertical ZnO nanorod arrays with high conductivity on an in situ Gd nanolayer. *RSC Adv.* **2015**, *5* (115), 94670−94678.
(22) Kisielowski, C.; Krüger, J.; Ruvimov, S.; Suski, T.; Ager, J., III; Jones, E.; Liliental-Weber, Z.; Rubin, M.; Weber, E.; Bremser, M.; Davis, R. F. Strain-related phenomena in GaN thin films. *Phys. Rev. B* **1996**, *54* (24), 17745.
(23) Kumar, R.; Kumar, R.; Panda, D.; Biswas, M.; Upadhyay, S.; Das, D.; Zhao, S.; Mi, Z.; Chakrabarti, S. Gallium Nitride Materials and Devices XIV. In In *Enhanced Optical and Structural Properties of MBE-Grown AlGaN Nanowires on Si Substrate by H-Ion Implantation and UV Ozone Treatment*; International Society for Optics and Photonics, 2019.
(24) Yeom, B.-R.; Navamathavan, R.; Park, J.-H.; Ra, Y.-H.; Lee, C.-R. Growth behavior of GaN epilayers on Si (111) grown by GaN nanowires assisted epitaxial lateral overgrowth. *CrystEngComm* **2012**, *14* (17), 5558−5563.
(25) Malard, L.; Pimenta, M.; Dresselhaus, G.; Dresselhaus, M. Raman spectroscopy in graphene. *Phys. Rep.* **2009**, *473* (5−6), 51−87.
(26) Pak, Y.; Mitra, S.; Alaal, N.; Xin, B.; Lopatin, S.; Almalawi, D.; Min, J.-W.; Kim, H.; Kim, W.; Jung, G.-Y.; Roqan, I. S. Dark-current reduction accompanied photocurrent enhancement in p-type MnO quantum-dot decorated n-type 2D-MoS2-based photodetector. *Appl. Phys. Lett.* **2020**, *116* (11), No. 112102, DOI: 10.1063/1.5143578.
(27) Zhu, J.; Tang, Y.; Yang, C.; Wang, F.; Cao, M. Composites of TiO2 nanoparticles deposited on Ti3C2 MXene nanosheets with enhanced electrochemical performance. *J. Electrochem. Soc.* **2016**, *163* (5), A785−A791.
(28) Almalawi, D. R. Investigating Novel Methods for Developing GaN Nanowire-based Devices Fabricated by Laser Ablation and via Material Hybridization for Optoelectronic Applications, Ph.D. Dissertation, King Abdullah University of Science and Technology (KAUST), 2020.
(29) *Transmission Electron Microscopy, A Textbook for Materials Science*, 2nd ed.; Williams, D. B., Ed.; Springer: New York, 2009.
(30) Hass, G.; Francombe, M. H.; Hoffman, R. W., *Physics of Thin Films: Advances in Research and Development*. Elsevier: 1966.
(31) Koch, R. The intrinsic stress of polycrystalline and epitaxial thin metal films. *J. Phys.: Condens. Matter* **1994**, *6* (45), 9519.
(32) Dalpian, G. M.; Chelikowsky, J. R. Self-purification in semiconductor nanocrystals. *Phys. Rev. Lett.* **2006**, *96* (22), No. 226802.
(33) Cao, G., *Nanostructures & Nanomaterials: Synthesis, Properties & Applications*. Imperial College Press: 2004.
(34) Yuan, X.; Yang, J.; He, J.; Tan, H. H.; Jagadish, C. Role of surface energy in nanowire growth. *J. Phys. D: Appl. Phys.* **2018**, *51* (28), No. 283002.
(35) Korotkov, R.; Niu, F.; Gregie, J.; Wessels, B. Investigation of the defect structure of GaN heavily doped with oxygen. *Physica B* **2001**, *308−310*, 26−29.
(36) Alwadai, N.; Mitra, S.; Hedhili, M. N.; Alamoudi, H.; Xin, B.; Alaal, N.; Roqan, I. S. Enhanced-performance self-powered solar-blind UV-C photodetector based on n-ZnO quantum dots functionalized by p-CuO micro-pyramids. *ACS Appl. Mater. Interfaces* **2021**, *13* (28), 33335−33344.
(37) Yan, M.; Zhang, H.; Widjaja, E.; Chang, R. P. Self-assembly of well-aligned gallium-doped zinc oxide nanorods. *J. Appl. Phys.* **2003**, *94* (8), 5240−5246.
(38) Fernández-Garrido, S.; Grandal, J.; Calleja, E.; Sánchez-García, M.; López-Romero, D. A growth diagram for plasma-assisted molecular beam epitaxy of GaN nanocolumns on Si (111). *J. Appl. Phys.* **2009**, *106*, No. 126102, DOI: 10.1063/1.3267151.
(39) Auzelle, T.; Haas, B.; Minj, A.; Bougerol, C.; Rouvière, J.-L.; Cros, A.; Colchero, J.; Daudin, B. The influence of AlN buffer over the polarity and the nucleation of self-organized GaN nanowires. *J. Appl. Phys.* **2015**, *117* (24), No. 245303.
(40) Reshchikov, M. A.; Morkoç, H. Luminescence properties of defects in GaN. *J. Appl. Phys.* **2005**, *97* (6), 061301.
(41) Pankove, J. I.; Moustakas, T. D.*Gallium Nitride (GaN)*; Elsevier, 1998.
(42) Li, Y.-T.; Han, C. F.; Lin, J.-F. Effects of nitrogen/oxygen on the electrical and optical properties and microstructure of triple layer AZO/Ag/AZO thin films. *Opt. Mater. Express* **2020**, *10* (2), 249−267.
(43) Inguva, S.; Vijayaraghavan, R. K.; McGlynn, E.; Mosnier, J.-P. Highly transparent and reproducible nanocrystalline ZnO and AZO thin films grown by room temperature pulsed-laser deposition on flexible Zeonor plastic substrates. *Mater. Res. Express* **2015**, *2* (9), No. 096401.
(44) Humphreys, F. J.; Hatherly, M., *Recrystallization and Related Annealing Phenomena*. Elsevier: 2012.
(45) Hu, J.; Zhang, J.; Wang, X.; Luo, J.; Zhang, Z.; Shen, Z., *A General Mechanism of Grain Growth-II: Experimental*. Elsevier Amsterdam, The Netherlands: 2021.
(46) Shkondin, E.; Takayama, O.; Panah, M. A.; Liu, P.; Larsen, P. V.; Mar, M. D.; Jensen, F.; Lavrinenko, A. Large-scale high aspect ratio Al-doped ZnO nanopillars arrays as anisotropic metamaterials. *Opt. Mater. Express* **2017**, *7* (5), 1606−1627.

https://doi.org/10.1021/acsomega.3c06302
ACS Omega 2023, 8, 46804−46815

(47) Zhang, Z.; Xu, X.; Qiu, L.; Wang, S.; Wu, T.; Ding, F.; Peng, H.; Liu, K. The way towards ultrafast growth of single-crystal graphene on copper. *Adv. Sci.* **2017**, *4* (9), No. 1700087.
(48) Race, C. P.; Hadian, R.; von Pezold, J.; Grabowski, B.; Neugebauer, J. Mechanisms and kinetics of the migration of grain boundaries containing extended defects. *Phys. Rev. B* **2015**, *92* (17), No. 174115.
(49) Dreyer, C. E.; Janotti, A.; Van de Walle, C. G. Absolute surface energies of polar and nonpolar planes of GaN. *Phys. Rev. B* **2014**, *89* (8), No. 081305.
(50) Foxon, C.; Novikov, S.; Hall, J.; Campion, R.; Cherns, D.; Griffiths, I.; Khongphetsak, S. A complementary geometric model for the growth of GaN nanocolumns prepared by plasma-assisted molecular beam epitaxy. *J. Cryst. Growth* **2009**, *311* (13), 3423−3427.
(51) Ristić, J.; Calleja, E.; Fernández-Garrido, S.; Cerutti, L.; Trampert, A.; Jahn, U.; Ploog, K. H. On the mechanisms of spontaneous growth of III-nitride nanocolumns by plasma-assisted molecular beam epitaxy. *J. Cryst. Growth* **2008**, *310* (18), 4035−4045.
(52) Klug, H. P.; Alexander, L. E.*X-Ray Diffraction Procedures for Polycrystalline and Amorphous Materials*; ACS, 1974.
(53) Consonni, V. Self-induced growth of GaN nanowires by molecular beam epitaxy: A critical review of the formation mechanisms. *Phys. Status Solidi RRL* **2013**, *7* (10), 699−712.
(54) Lorenz, K.; Miranda, S.; Alves, E.; Roqan, I. S.; O'Donnell, K.; Boćkowski, M. Gallium Nitride Materials and Devices VII. In *High Pressure Annealing of Europium Implanted GaN*; SPIE, 2012; pp 49−54.
(55) Chin, A. H.; Ahn, T. S.; Li, H.; Vaddiraju, S.; Bardeen, C. J.; Ning, C.-Z.; Sunkara, M. K. Photoluminescence of GaN nanowires of different crystallographic orientations. *Nano Lett.* **2007**, *7* (3), 626−631.
(56) Calabrese, G.; van Treeck, D.; Kaganer, V.; Konovalov, O.; Corfdir, P.; Sinito, C.; Geelhaar, L.; Brandt, O.; Fernández-Garrido, S. Radius-dependent homogeneous strain in uncoalesced GaN nanowires. *Acta Mater.* **2020**, *195*, 87−97.
(57) Schubert, E. F.; Goepfert, I.; Grieshaber, W.; Redwing, J. Optical properties of Si-doped GaN. *Appl. Phys. Lett.* **1997**, *71* (7), 921−923.
(58) Meister, D.; Böhm, M.; Topf, M.; Kriegseis, W.; Burkhardt, W.; Dirnstorfer, I.; Rösel, S.; Farangis, B.; Meyer, B.; Hoffmann, A.; et al. A comparison of the Hall-effect and secondary ion mass spectroscopy on the shallow oxygen donor in unintentionally doped GaN films. *J. Appl. Phys.* **2000**, *88* (4), 1811−1817.
(59) Okada, N.; Tadatomo, K.; Yamane, K.; Mangyo, H.; Kobayashi, Y.; Ono, H.; Ikenaga, K.; Yano, Y.; Matsumoto, K. Performance of InGaN/GaN light-emitting diodes grown using NH3 with oxygen-containing impurities. *Jpn. J. Appl. Phys.* **2014**, *53* (8), No. 081001.
(60) Roqan, I. S.; O'Donnell, K.; Martin, R.; Edwards, P.; Song, S.; Vantomme, A.; Lorenz, K.; Alves, E.; Boćkowski, M. Identification of the prime optical center in GaN: Eu 3+. *Phys. Rev. B* **2010**, *81* (8), No. 085209.
(61) Debnath, R. K.; Meijers, R.; Richter, T.; Stoica, T.; Calarco, R.; Lüth, H. Mechanism of molecular beam epitaxy growth of GaN nanowires on Si(111). *Appl. Phys. Lett.* **2007**, *90* (12), No. 123117.
(62) Rashba, E. Giant oscillator-strengths associated with exciton complexes. *Sov. Phys. Semicond. USSR* **1975**, *8* (7), 807−816.
(63) Almalawi, D.; Lopatin, S.; Mitra, S.; Flemban, T.; Siladie, A.-M.; Gayral, B.; Daudin, B.; Roqan, I. S. Enhanced UV emission of GaN nanowires functionalized by wider band gap solution-processed p-MnO quantum dots. *ACS Appl. Mater. Interfaces* **2020**, *12* (30), 34058−34064.
(64) Ajia, I. A.; Yamashita, Y.; Lorenz, K.; Muhammed, M.; Spasevski, L.; Almalawi, D.; Xu, J.; Iizuka, K.; Morishima, Y.; Anjum, D.; Roqan, I. S.; et al. GaN/AlGaN multiple quantum wells grown on transparent and conductive (−201)-oriented β-Ga2O3 substrate for UV vertical light emitting devices. *Appl. Phys. Lett.* **2018**, *113* (8), No. 082102.
(65) Ajia, I. A.; Almalawi, D.; Lu, Y.; Lopatin, S.; Li, X.; Liu, Z.; Roqan, I. S. Subquantum-well influence on carrier dynamics in high efficiency DUV dislocation-free AlGaN/AlGaN-based multiple quantum wells. *ACS Photonics* **2020**, *7* (7), 1667−1675.
(66) Ajia, I. A.; Edwards, P. R.; Pak, Y.; Belekov, E.; Roldan, M. A.; Wei, N.; Liu, Z.; Martin, R. W.; Roqan, I. S. Generated Carrier Dynamics in V-Pit-Enhanced InGaN/GaN Light-Emitting Diode. *ACS Photonics* **2018**, *5* (3), 820−826.
(67) Hammersley, S.; Watson-Parris, D.; Dawson, P.; Godfrey, M.; Badcock, T.; Kappers, M. J.; McAleese, C.; Oliver, R. A.; Humphreys, C. J. The consequences of high injected carrier densities on carrier localization and efficiency droop in InGaN/GaN quantum well structures. *J. Appl. Phys.* **2012**, *111* (8), No. 083512.
(68) Dai, Q.; Shan, Q.; Cho, J.; Schubert, E. F.; Crawford, M. H.; Koleske, D. D.; Kim, M.-H.; Park, Y. On the symmetry of efficiency-versus-carrier-concentration curves in GaInN/GaN light-emitting diodes and relation to droop-causing mechanisms. *Appl. Phys. Lett.* **2011**, *98* (3), No. 033506.
(69) Muhammed, M. M.; Alwadai, N.; Lopatin, S.; Kuramata, A.; Roqan, I. S. High-Efficiency InGaN/GaN Quantum Well-Based Vertical Light-Emitting Diodes Fabricated on β-Ga2O3 Substrate. *ACS Appl. Mater. Interfaces* **2017**, *9* (39), 34057−34063.
(70) Seong, T. Y.; Han, J.; Amano, H.; Morkoç, H. *III − Nitride Based Light Emitting Diodes and Applications*; Springer: Dordrecht, 2013; Vol. *126*, p 171.

https://doi.org/10.1021/acsomega.3c06302
ACS Omega 2023, 8, 46804−46815